Meteorologische Zeitschrift, PrePub DOI 10.1127/metz/2014/0609

Numerical simulations of baroclinic driven flows in a thermally driven rotating annulus using the immersed boundary method

Thomas von Larcher[1]* and Andreas Dörnbrack[2]

[1]Freie Universität Berlin, Institute for Mathematics, Germany
[2]German Aerospace Center, Institute of Atmospheric Physics, Oberpfaffenhofen-Wessling, Germany

(Manuscript received April 16, 2014; in revised form July 17, 2014; accepted August 11, 2014)

Abstract

We present results of numerical simulations of baroclinic driven flows in the thermally driven rotating annulus using the immersed boundary method for modeling of the boundary conditions. The Navier-Stokes equations in the Boussinesq approximation are solved in the Eulerian flux-form advection scheme with the geophysical flow solver EULAG as numerical framework. We test our approach against results of an appropriate laboratory experiment with water as working fluid and directly aim at the wavy flow regime where complex flows and regular wave patterns are generally observed but where centrifugal effects and turbulence is of minor importance. Multivariate statistical methods are used for analyzing time series of computed temperature data. We, here, present the outcome of the time series data analysis at particular parameter points, and specifically analyze a complex wave-wave interaction, and, secondly, a wave mode switch where the azimuthal wave number changes to the next higher one. The numerical results are highly consistent with the experimental observations. That encourage us to focus on our actual goal as the next step, that is the irregular flow regime found at large rotation rates where the centrifugal force has an increasing effect on flow states and where multiple scale flows are generally observed.

Keywords: baroclinic driven flows, thermally driven rotating annulus, numerical experiments, immersed boundary method, complex flow regimes, multivariate time series analysis

1 Introduction

In the work presented here, we focus on a numerical study on computing baroclinic waves in the well-known rotating thermally driven annulus with respect to a reference experiment. The reference experiment under consideration is involved in the long-term priority programme MetStroem and hosted at the Brandenburg University of Technology Cottbus-Senftenberg, Germany. A number of experiments were performed in the Cottbus experiment in the past decade. E.g., von Larcher and Egbers (2005a) focused in particular on the underlying dynamics of complex flows, von Larcher and Egbers (2005b) studied transitions of azimuthal wave patterns with respect to the radius ratio, Harlander et al. (2011) focused specifically on wave interactions, Harlander et al. (2012) studied the flow in a partially blocked set-up, Seelig et al. (2013) presented a study on singular vector growth, and Vincze et al. (2014b) investigated flow patterns with a sloping bottom topography.

The model set-up, Fig. 1, generally consists of a cylindrical gap rotating uniformly around its vertical axis of symmetry. A radial temperature difference is realized by heating (cooling) the outer (inner) vertical sidewall. Typically, the model is provided either with an upper free surface or with an upper rigid lid. Our research cavity has a gap width of 0.075 m with inner radius $a = 0.045$ m and outer radius of $b = 0.120$ m, and the fluid depth is $d = 0.135$ m, with a free top surface, cf. von Larcher and Egbers (2005b).

The flow regimes that developed in the research cavity for a given fluid are driven by the rotation rate and by the radial temperature gradient, and the overall regime diagram generally separates in three distinct regions, that is the basic flow regime at relative low rotation rates, the anvil-shape region of the wavy flow regime where steady and time-dependent flow patterns of baroclinic waves occur, and the irregular flow regime at relative high rotation rates (e.g., Fowlis and Hide (1965)). Depending on its physical characteristic, generally nonlinear, those time-dependent flows are termed amplitude vacillations, e.g., Hignett (1985), Lu and Miller (1997), Pedlosky (1970), and shape vacillations, e.g., Read (1992). The above mentioned particular regions in the regime diagram reveal further remarkable flow characteristics as e.g., weak waves, dispersive waves, etc. See e.g., Früh and Read (1997) for research on the first transition from basic flow to wavy flow regime, and e.g., Read et al. (1992) for study on quasi-periodic

*Corresponding author: Thomas von Larcher, Institute for Mathematics, Freie Universität Berlin, Arnimallee 6, 14195 Berlin, Germany, e-mail: larcher@math.fu-berlin.de

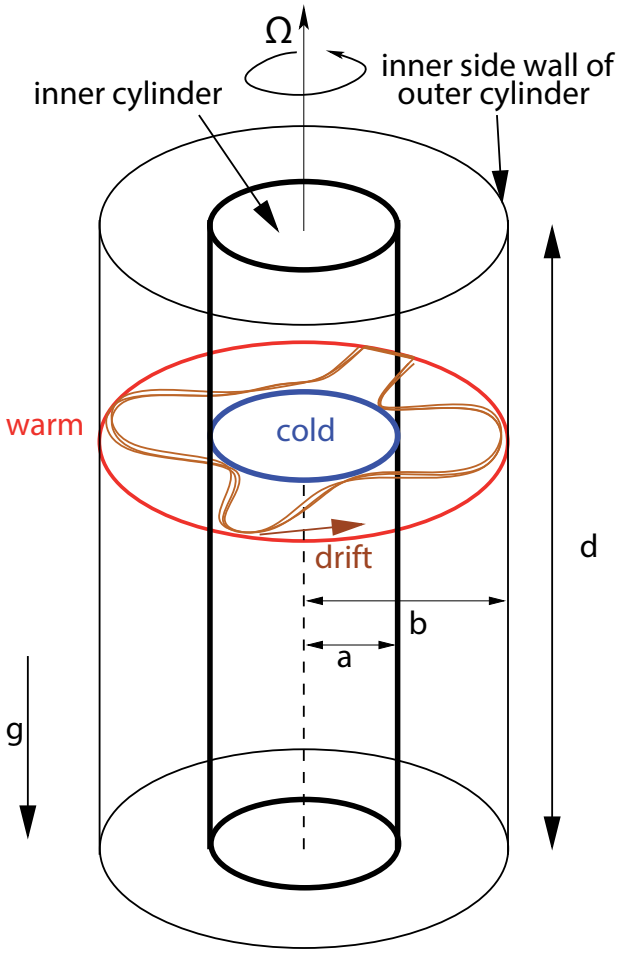

Figure 1: Sketch of the model set-up, according to Figure 2 of VON LARCHER and EGBERS (2005b), g as the vector of gravitational acceleration.

and chaotic flow regimes, and e.g., MORITA and URYU (1989), PFEFFER et al. (1997) for a study on geostrophic turbulence naturally found at high rotation rates. Apart from the fluid dynamics phenomena, the set-up has been accepted as an elegant laboratory experiment for studying principles of atmospheric flows, cf. e.g. FULTZ et al. (1959), FULTZ (1961), HIDE (1969), and the review article by HIDE and MASON (1975) as well as the already mentioned article by READ et al. (1992).

Even if it is under consideration since the late 1950s when R. HIDE and D. FULTZ conducted independently the first principal investigations, e.g., FULTZ (1951) and HIDE (1958), the annulus is still of interest in recent research on atmospheric flow and basic fluid dynamics as well as for validating CFD codes which incorporate new numerical concepts. The latter might be due to the relative simple geometry of the annulus with well defined boundary conditions whereas the flow patterns that are observed show a multifaceted behavior as described above. It should be mentioned here, that F. VETTIN introduced principals of the experimental set-up already in 1884 in a paper published in *Meteorologische Zeitschrift*, cf. VETTIN (1884).

The EULAG framework is a multipurpose multiscale solver for all-scale geophysical flows, see PRUSA et al. (2008) for a comprehensive overview of the framework. EULAG is based on the non-hydrostatic anelastic fluid equations of motion, cf. e.g. GRABOWSKI and SMOLARKIEWICZ (2002) for a multiscale anelastic model for meteorological research, that can be solved either in Eulerian flux form or in semi-Lagrangian advective form, and it allows for a number of assumptions for particular flow characteristics, specifically the compressible/incompressible Boussinesq approximation, incompressible Euler/Navier-Stokes equations, and fully compressible Euler equations. The governing partial differential equations are evaluated with a remarkable semi-implicit non-oscillatory forward-in-time (NFT) algorithm and a finite volume discretization, SMOLARKIEWICZ (1991), SMOLARKIEWICZ and MARGOLIN (1997), SMOLARKIEWICZ and MARGOLIN (1998). EULAG has been successfully applied to a number of geophysical problems, documented by the enormous number of publications in the past years (cf. the list of publications with respect to applications on its website http://www.mmm.ucar.edu/eulag/pub_appl.html) ranging from cloud microscale to synoptic and global scale in atmospheric flows, as well as it was used for modeling oceanic flows. It is worth mentioning that also solar convection, e.g., ELLIOTT and SMOLARKIEWICZ (2002), and urban flows, SCHRÖTTLE and DÖRNBRACK (2013), were studied successfully with this numerical code, and beyond geoscience phenomena, EULAG has been also applied for simulating waves in the human brain, COTTER et al. (2002).

Besides the possibility to consider particular approximations in flow characteristics as mentioned above, EULAG also provides a framework for Direct Numerical Simulation (DNS), Large Eddy Simulation (LES), and implicit LES (ILES). Having future works in the turbulent flow regime of the baroclinic annulus in mind, it is, therefore, reasonable to use the EULAG framework for our purposes, too.

2 The model and governing equations

Even if EULAG is a highly flexible framework, it is originally written for research on geophysical flows on rotating planets. To implement our model set-up, that is the rotating annulus, we, therefore, have to adapt the framework for our needs. We use a Cartesian (x, y, z) domain with physical lengths 0.258×0.258 m in x- and y-direction and 0.135 m in z-direction where z is the height. The (static) grid dimension is $192 \times 192 \times 67$ in x, y, z. That results in a grid resolution of 0.134×10^{-2} in x, y-direction and 0.204×10^{-2} in z-direction. In this Cartesian domain, the annulus geometry is defined with inner radius of 0.045 m and outer radius of 0.12 m by using the usual conversion from Cartesian to Polar coordinates.

The sidewalls and the end walls of the annulus are modeled with the immersed boundary approach

(cf. Goldstein et al. (1993)). In this method, fictitious body forces are incorporated in the governing equation of motion to represent no-slip boundaries which leads to a damping of the solution in an appropriate time interval. We refer the reader to Smolarkiewicz et al. (2007) for a comprehensive presentation of the immersed boundary approach in the EULAG flow solver. Also, e.g. Mittal and Iaccarino (2005) gives a thorough review of immersed boundary methods. In our study, the damping parameters are set so that the motion at the boundaries is damped to zero within a single time step.

At the bottom end wall, no-slip conditions are set as well, i.e. $\vec{U} = (u, v, w) = 0$, with $\vec{U}$ as the velocity vector, (u, v) as its horizontal components and w as its vertical component. At the upper end wall, only the vertical velocity component is bounded as $w = 0$.

The temperature difference $\Delta T = T_{\max} - T_{\min}$, with $T_{\max} = +\frac{\Delta T}{2}$ and $T_{\min} = -\frac{\Delta T}{2}$ relative to a reference temperature, is realized by setting $T = T_{\max}(T_{\min})$ where the radius is equal or greater (lower) than the outer (inner) radius. Rotation is implemented with the Coriolis parameter by default. We, here, set the horizontal component of the Coriolis force to zero and the vertical component to the magnitude of the Coriolis parameter as the annulus rotates uniformly around its vertical axis of symmetry. Note, that we found that the (numerical) Coriolis parameter must be scaled by a factor of $0.5 \times \frac{60}{2\pi} \approx 4.77$ with respect to rotation rates set in the reference experiment. However, this specific factor apparently comes out from the EULAG code. This factor must then also be taken into account for calculating drift rates of the computed wave patterns.

In all computations that are presented here, the time step increment is set to 2.5×10^{-3} s to ensure a small CFL-number, $\mathrm{CFL} = U \cdot \frac{\Delta t}{\Delta x}$. The computed data are stored every 2000 time steps, i.e. every 5 s. The reference temperature is 20 °C and the temperature difference between the inner and outer layer is 8 K. Note, that this temperature difference is kept fix and only the rotation rate is varied in all computations. Thus, regarding the dimensionless numbers, discussed in the next section, that results in keeping the Rayleigh number fix but varying the thermal Rossby number, and the Taylor number, of course.

2.1 Governing equations

We, here, describe to some extent principles of the governing equations that determine the flow under consideration as we feel that this would gain a better understanding of the underlying physics. The non-hydrostatic anelastic equations implemented in EULAG are described in detail in Smolarkiewicz and Margolin (1997).

The governing equations that describe the flow in the thermally driven rotating annulus in good approximation are the Navier-Stokes equations for an incompressible fluid in the Boussinesq approximation in which variations of density are neglected except in the buoyancy term. In their non-dimensional form, the equations read

$$\partial_t \vec{U} + \vec{U} \cdot \nabla \vec{U} + \sqrt{Ta}\, \hat{e}_z \times \vec{U} = -\nabla p + \nabla^2 \vec{U} + Ra \frac{1}{Pr} \Theta \hat{e}_z + \alpha \Delta T \frac{Ta}{4} s \hat{e}_s \quad (2.1)$$

$$\partial_t \Theta + \vec{U} \cdot \nabla \Theta = \frac{1}{Pr} \nabla^2 \Theta \quad (2.2)$$

$$\nabla \cdot \vec{U} = 0 \quad (2.3)$$

in cylindrical coordinates (s, ϕ, z), s (z) as radial (vertical) direction and ϕ as azimuthal direction, with the non-dimensional parameters

$$Ta = \frac{f^2 L^4}{\nu^2} = \frac{4\Omega^2 (b-a)^4}{\nu^2}, \quad (2.4)$$

$$Ra = \frac{\alpha \Delta T g L^3}{\nu \kappa} = \frac{\alpha \Delta T g (b-a)^3}{\nu \kappa}, \quad (2.5)$$

$$Pr = \frac{\nu}{\kappa}, \quad (2.6)$$

where Ta is the Taylor number, Ra is the Rayleigh number, and Pr is the Prandtl number. $\hat{e}_z$ is the unit vector in the direction of rotation, and $f = 2\Omega$ is the Coriolis parameter. Length has been scaled by the gap width $(L = b - a)$, time by the viscous diffusion time $\frac{(b-a)^2}{\nu}$, U by $\left(\frac{\nu}{(b-a)}\right)$, and T by ΔT.

(2.1) includes the centrifugal term, the last term on the right hand side, which is an extra forcing term in the s-component of the momentum equation. If a free top surface is assumed, the centrifugal force could principally cause a deflection of the surface to form a paraboloid rather than a flat surface. However, such a surface deflection was generally not observed in the reference experiments as long as g, the acceleration due to gravity, is much larger than the centrifugal acceleration, $\Omega^2 s$. The Froude number, $Fr = \frac{g}{\Omega^2 s}$, defines the ratio of both forces. Note, that the magnitude of the Froude number is radius dependent. The influence of centrifugal effects on flow patterns with respect to the Froude number is discussed by e.g. Read et al. (2008). With respect to the reference experiment, we refer to Harlander et al. (2011) and von Larcher et al. (2013) for a more closely analysis on the influence of the centrifugal force on the top surface. The Rayleigh number, (2.5), measures the thermal forcing (α as the volumetric expansion coefficient of the fluid), and the Prandtl number measures material properties of the fluid, specifically the ratio of the viscosity, ν, to the thermal diffusivity, κ. We will choose the Prandtl number to $Pr = 7.0$, as in the reference experiment. Note, that Pr is kept fix in our study.

The three non-dimensional numbers, together with the two geometrical parameters defining the shape of the research cavity, i.e. the radius ratio $\eta = \frac{a}{b}$, and the aspect ratio $\Gamma = \frac{d}{(b-a)}$, specify the problem.

Note, that for historical reasons studies on the thermally driven rotating annulus usually do not deal with

the Rayleigh number directly, but rather with a parameter known as the thermal Rossby number, defined as

$$Ro_T = 4 \times \frac{Ra\,\Gamma}{Pr\,Ta} = \frac{g\alpha\Delta T d}{\Omega^2(b-a)^2}. \tag{2.7}$$

The thermal Rossby number is related to the usual Rossby number, $Ro = \frac{U}{fL}$, by the scaling velocity, $U = \frac{g\alpha\Delta T d}{fL}$, which comes out from the thermal wind relation. Similar, the Taylor number is often modified by incorporating the aspect ratio, Γ, and the modified Taylor number then reads

$$\widetilde{Ta} = \frac{4\Omega^2(b-a)^4}{\nu^2} \times \frac{1}{\Gamma} = \frac{4\Omega^2(b-a)^5}{\nu^2 d}. \tag{2.8}$$

We emphasise that Ro_T is not a new parameter but a rescaled version of the Rayleigh number. However, we will follow the historical path and will present our results in terms of $\widetilde{Ta}$ and Ro_T.

3 Data processing and multivariate data analysis

As already mentioned, we directly aim at investigating complex flows which are usually triggered by the interaction of different wave numbers or by interaction of the zonal mean flow and wave flows. To detect those oscillating patterns, we apply the Multichannel Singular System Analysis (M-SSA) method to our data. The M-SSA is an extension of the single-channel SSA. SSA, in general, is a statistical time series analysis technique to detect the variability of flow fields, Elsner and Tsonis (1996), and the extension of single channel SSA to multichannel SSA was first noted by Broomhead and King (1986a) and by Broomhead and King (1986b), and regarding the baroclinic annulus under consideration, M-SSA has been first introduced by Read (1993) who applied that data analysis technique to time series of temperature data. M-SSA has been also applied by Harlander et al. (2011) particularly to analyze noisy time series of velocity data measured in the irregular flow regime at higher rotation rates.

(M-)SSA is similar to Empirical Orthogonal Functions (EOF) analysis, the method of choice in geosciences. Both methods, classical EOF and SSA, search for patterns that explain a great portion of variability of time series under consideration. In fact, Vautard and Ghil (1989) mentioned the possibility to link individual EOFs, as an outcome in the SSA, to physical patterns by looking for pairs of eigenvectors in quadrature. Due to the great relevance in discrimination between signal and noise in time series data, e.g., Mann and Lees (1996), considerable attention has been attained to these methods in the past, cf. e.g., Allen and Smith (1996) for a list of various applications of those methods in geosciences and climatology.

In our study, we use the Singular Spectrum Analysis - Multi Taper Method (SSA-MTM) toolkit, an open source software originally developed at University of California Los Angeles (UCLA), Dettinger et al. (1995) and Ghil et al. (2002), for analyzing the outcome of our numerical computations, i.e. time series of temperature data. As mentioned in Vautard et al. (1992), this toolkit is particularly suited to analyze short and noisy time series. Moreover, the SSA-MTM toolkit not only allows for the construction of principal components but also for the reconstruction of the original multichannel time series data matrix. In the following, we summarize principles of the procedures but refer the reader to the references given in this section as well to the corresponding Website (http://www.atmos.ucla.edu/tcd/ssa/) for a detailed description of the theory and for some demonstrations.

Applying SSA to a time series of data contains three elementary steps. First, the time series

$$\{x(t) : t = 1, \dots N\} \tag{3.1}$$

is embedded in a vector space of dimension M by constructing M lagged copies of $x(t)$:

$$\{x(t-j) : j = 1, \dots M\}. \tag{3.2}$$

Note, that M is usually denoted as the window length. Secondly, the lag-covariance matrix $M \times M$ of the data is computed and a matrix estimator C_D is defined. We use the algorithm by Vautard and Ghil (1989), which is implemented in the toolkit, where C_D is directly estimated from the data as a Toeplitz matrix with constant diagonals. Finally, the lag-covariance matrix is diagonalized and the eigenvalues $\{\lambda_k : 1 \le k \le M\}$ are ranked in decreasing order. The eigenvalues then represent the variance of the time series in the direction of the respective eigenvectors E_k which are often called EOFs.

Time series of the eigenvectors can be constructed called principal components (PC). These PCs give the projection of the data matrix onto the respective EOF. The construction of the k-th PC reads

$$A_k(t) = \sum_{k=1}^{M} x(t+j)E_{k,j}, \quad t = 0, \dots, N-M, \tag{3.3}$$

where $\{E_{k,j} : j = 1, \dots, M\}$. The PCs are of length $N' = N - M$. As an extension, the time series $x(t)$ can be partially reconstructed up to its original length N by a combination of a subset of eigenelements K:

$$R_K(t) = \frac{1}{M_\tau} \sum_{k \in K} \sum_{j=1}^{M} A_k(t-j)E_{k,j}, \quad M \le t \le N'. \tag{3.4}$$

Thus, $R_K(t)$ incorporates a combination of K-PCs. Note, that $M_\tau = M$ at the central part of the time series but $M_\tau = \min\{t, N-t+1\}$ close to the endpoints, see Vautard et al. (1992) for details. In case K consists of a single eigenvector E_k, $R_K(t)$ is the k-th reconstructed component $x_k(t)$. Summing up all reconstructed components,

Table 1: Azimuthal wave number, m, and drift rate, c, observed in run A–D of the numerical simulations, denoted by subscript (*num*), and in the laboratory experiment, subscript (*exp*). Ω as rotation rate, *Ta* as Taylor number, and Ro_T as thermal Rossby number. $2/3i$ denotes a wave-wave interaction of azimuthal wave number 2 and 3. Note, that the temperature difference, ΔT, was set to 8 K in all runs.

run	Ω [$\frac{rad}{s}$]	$\widetilde{Ta}$ [10^6]	Ro_T	$m_{(exp)}$	$m_{(num)}$	$c_{(exp)}$ [$\frac{rad}{s}$]	$c_{(num)}$ [$\frac{rad}{s}$]
A	0.314	6.89	3.95	2	$2/3i$	0.030	0.010
B	0.733	37.48	0.72	3 or 4	3 or 4	0.012 (3) / 0.009 (4)	0.012 (3) / 0.009 (4)
C	0.942	61.96	0.44	3 or 4	4	0.010 (3) / 0.009 (4)	0.007
D	1.780	221.06	0.12	4	4	0.004	0.004

the time series can be reconstructed in total, thus

$$x(t) = \sum_{k=1}^{M} x_k(t). \tag{3.5}$$

To analyze our numerically generated data with the M-SSA, a pre-processing procedure is needed. The data sets originally contain $192 \times 192 \times 67 = 2,469,888$ values per sample output. We first reduce the large data set and focus on individual time series taken from equidistant grid points at mid radius and at the top surface. In fact, we extract 47 equidistant channels covering the full circle in azimuth at mid radius from the data. The coordinates of the 47 mid radius grid points were computed from the original numerical Cartesian grid by conversion from Polar to Cartesian coordinates, where the x, y-coordinates were rounded to the nearest integer if needed. With this, we obtain a homogeneous data set with grid distance $\Delta\Phi = 7.6\,°$, Φ as the aziumth. Note, that the prime number has been chosen with intent as to avoid the possibility of artifacts in the M-SSA data analysis as mentioned earlier by Wolf-Gerrit Früh (private communication). However, we believe that there is no strict rule to use a prime number but at least an odd number of time series channels for the data matrix would be reasonable as the multiplication of neighbored integers (here wave numbers) results in an even integer.

The window length, M, is a crucial parameter as it sets the size of the autocovariance matrix to be constructed from the data. To test the robustness of our results with respect to M, we have applied different window sizes, a large and a small window size of e.g. in run A, $M = 38$ ($M = 9$) which is 10 % (2.4 %) of the total data samples. The outcome of those tests will be not discussed here specifically as both window sizes leads to nearly identical results.

4 Results

In the following, we present results found at four particular parameter points, here after referred to as run *A–D* (Table 1). To illustrate our findings, snapshots of the respective flow patterns observed at those runs are shown in Figs. 3–5. Those snapshots are outcomes of the post-processing procedure where time series of temperature and velocity data are generated.

Both, the wave number and the drift rate of the wave flow patterns could be easily determined by visual inspection of the time series of post-processed temperature and velocity images. Those results are given in Table 1, too, and for comparison also results of the reference experiment are given there.

We, first, summarize the general results found at parameter points *A–D* and will mention some specific results in more detail afterwards:

- At run A, a complex flow phenomena is observed that is a mode interaction of azimuthal wave number $m = 2$ and $m = 3$, usually denoted as $m = 2/3i$. Here, we found that the two modes of different wave number do coexist.
- At run B, C, and D, the computations reveal steady flow patterns of different azimuthal wave number m.
- At run B, the resulting flow regime depends on the initial state. If we start with a basic flow solution (computed previously at low rotation rate), much smaller than the reference rotation rate for run B, (cf. Fig. 2, right panel), and then increase the rotation rate to run B, a wave of wave number $m = 3$ established. In contrast, starting with the solution for a non-rotating case, i.e. $\Omega = 0$ (cf. Fig. 2, left panel), a $m = 4$ wave pattern is observed. The $m = 4$ mode is also observed when the solution of run D, located at a much higher Taylor number than run B, is used as initial sequence. Note, that in all computational runs the Taylor number is set by a sudden increase/decrease of the rotation rate, i.e. there is no time-dependent spin-up or spin-down of the rotation rate to the corresponding parameter point.
- At run C, the wave pattern that immediate develops after the initial phase is of wave number 3 but switches to a $m = 4$ mode after about 60 time steps which then remains the dominating mode.

Let us now consider the results that are found in run A and in run C in more detail. We here focus on the outcome of the data analysis with the M-SSA method, following the post-processing operations described in Sec. 3. Fig. 6 shows the results yielded for run A, and results of run C are given in Fig. 7.

For run A, the top left panel of Fig. 6 shows the time series of the temperature data. The wave pattern manifests at time step 52, approximately, and the onset of the wave flow is linked with a sudden increase of the

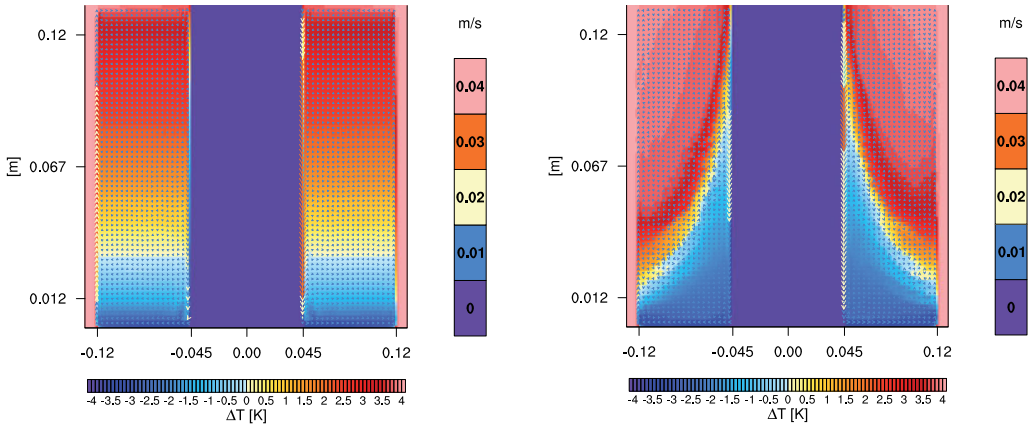

Figure 2: *x-z* cross-section of temperature difference (contours) and velocity field (vectors) at $\Omega = 0\,\mathrm{rad\,s^{-1}}$ (0 rpm) (left) and at $\Omega = 0.15\,\mathrm{rad\,s^{-1}}$ (1.47 rpm) (right). Note that the outer radius of the research cavity is 0.12 m and the height is 0.135 m.

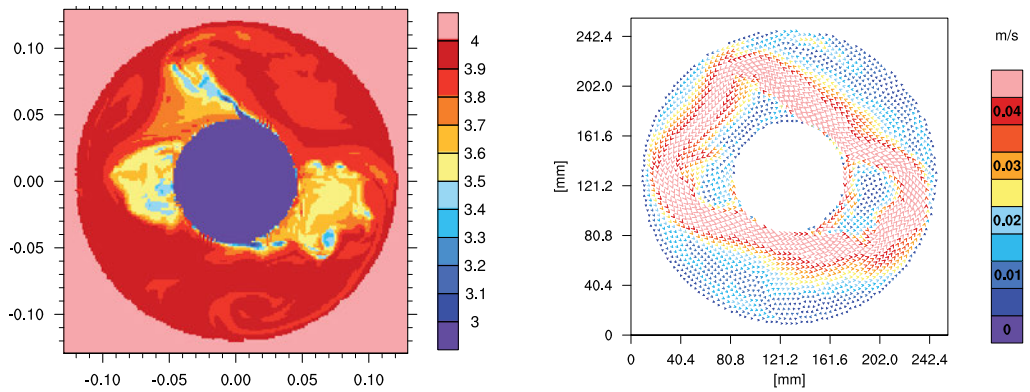

Figure 3: run *A*: *x-y* cross-section snapshot of temperature difference, unit [m] and [K], (left) and velocity field (right) computed at surface.

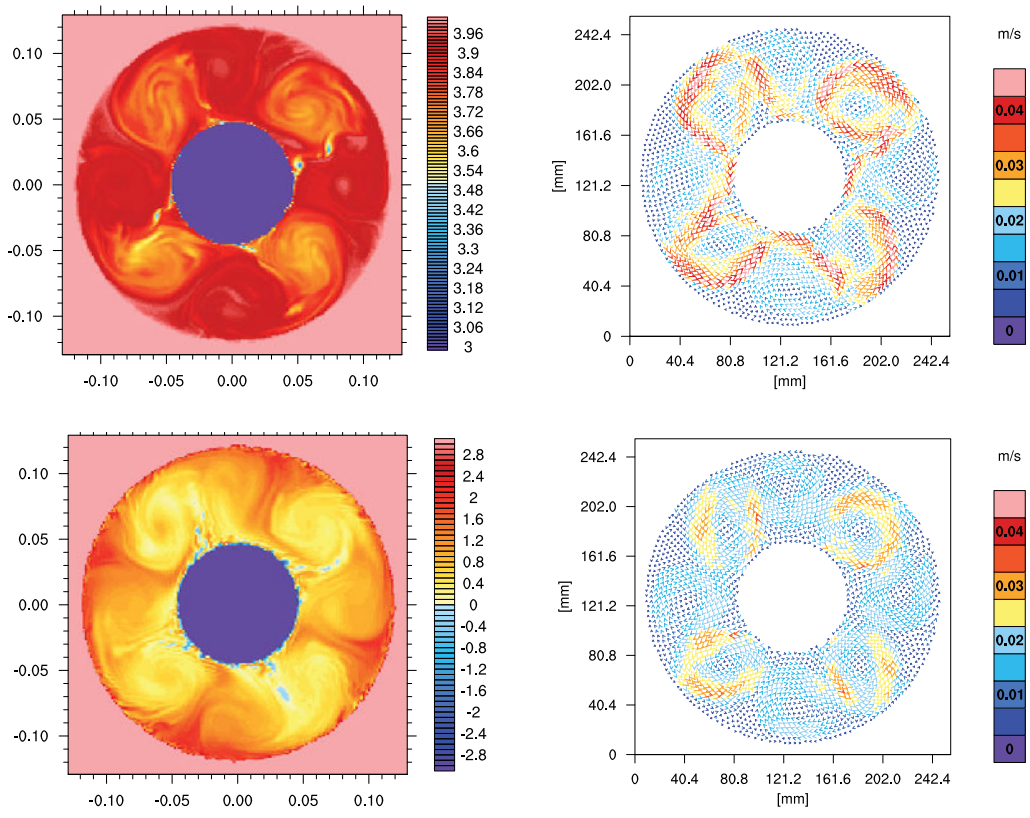

Figure 4: as Fig. 3 but for run *C*. *Top row:* at surface, *Bottom row:* between base and mid depth.

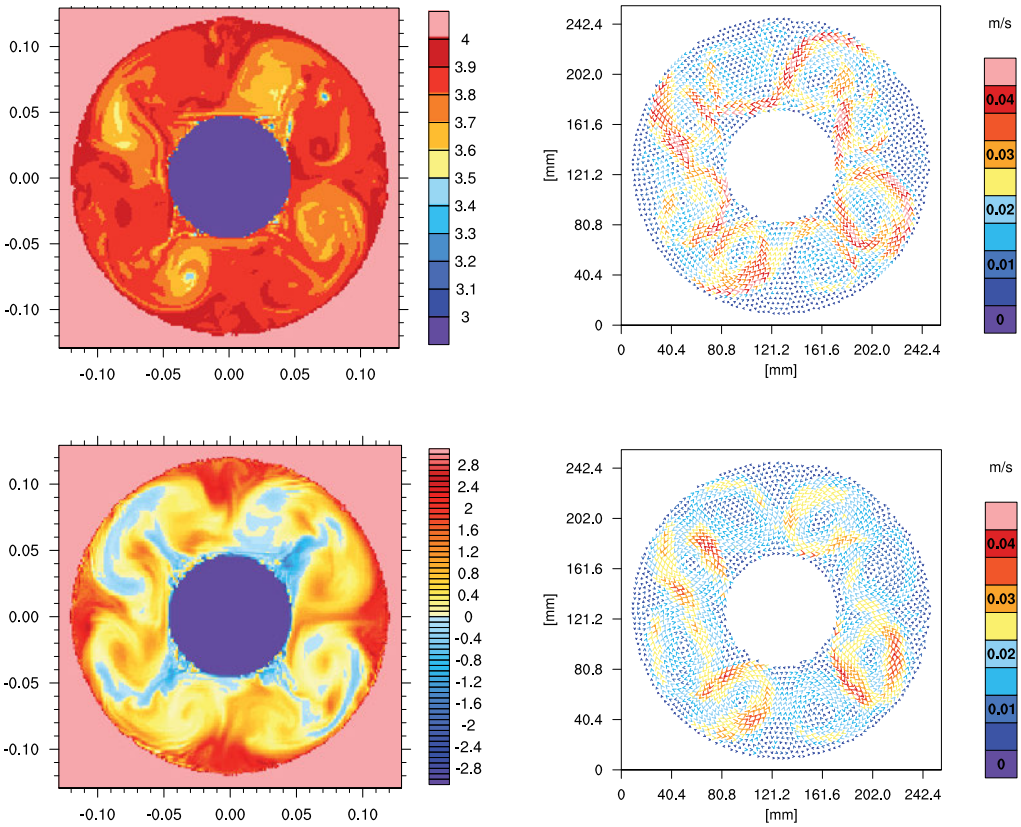

Figure 5: as in Fig. 4 but for run *D*.

temperature from about 3.7 K in the basic flow state to 3.9 K in the wave flow state. The eigenvalue (EV) spectrum of the first 20 eigenvalues (top right panel of Fig. 6) computed from that data time series matrix shows that the first eigenvalue pair, EV 1 and 2, incorporates about 39 % of the total variance. The second EV pair, EV 4 and 5, contains 7 % of the variance, and there are 3 other pairs each of according to amount nearly equal EVs, i.e. EV 6-11, before the noisy tail of the spectrum emerges. The time series of PC pair 1,2 for a single channel (center right) show the onset of the wave flow, beginning with a very small amplitude approximately at time step 52, wiggling around before a sudden increase of the amplitude. The time series of PC pair 4,5 shows the same behavior at the onset but in contrast to PC pair 1,2 the amplitude of that pattern is to a larger extent time-dependent. Its repeated intermittent bursting is correlated with the slight amplitude variations observed in the time series of PC pair 1,2. More precisely, PC pair 4,5 apparently increases at the cost of PC 1,2 and vice versa. The reconstruction of the multichannel data matrix with SSA components 1,2 (center left panel in Fig. 6) and components 4,5 (bottom left panel) reveal a wave of wave number 2 and of wave number 3, resp., whereas the latter apparently incorporates further oscillating features. Once settled, both oscillating patterns persist until computations are stopped. Note, that the three other pairs of nearly equal EV mentioned above, i.e. EV pair 6-11, are associated with multiples of the two modes, and we do not found further dominating modes.

Now, we turn to run *C* (cf. Fig. 7). Again, the top left panel shows the multichannel matrix that contains the 47 time series channels and covering the total output time steps. In addition, an extract of the data matrix focusing on the first 100 time steps is plotted, too. Starting from the basic flow solution computed at low rotation rate (Fig. 2, right panel), the onset of the wave flow is observed after 4 time steps and the wave pattern has settled after approx. 40 time steps. The EV spectrum of the data matrix (top right panel) shows a particular pair of eigenvalues (EV 1,2) which contains about 50 % of the total variance. The very next pair of nearly equal EV, pair 3,4, comprises about 5 % and thus a significant lower amount of variance. The single channel time series of PC pair 1,2 (center right panel in Fig. 7) reveals an oscillating pattern with a weak amplitude within the first 60 time steps at which it is established, and that pattern then persists throughout the computations. In contrast, the oscillating pattern linked with PC pair 3,4 (bottom right panel) dominates the first 50 time steps before its amplitude decreases considerably. Subsequently, the pattern is still alive but has a very weak amplitude. The multichannel reconstruction with SSA components 1,2 (center left panel) and components 3,4 (bottom left panel) shows that pair 1,2 is linked with a eve of wave number 4, and pair 3,4 is linked with a wave number 3 mode. As in the foregoing analysis of run *A*, further pairs of nearly equal EV, here EV pair 5,6 and 7,8, are associated with multiples of the two wave modes.

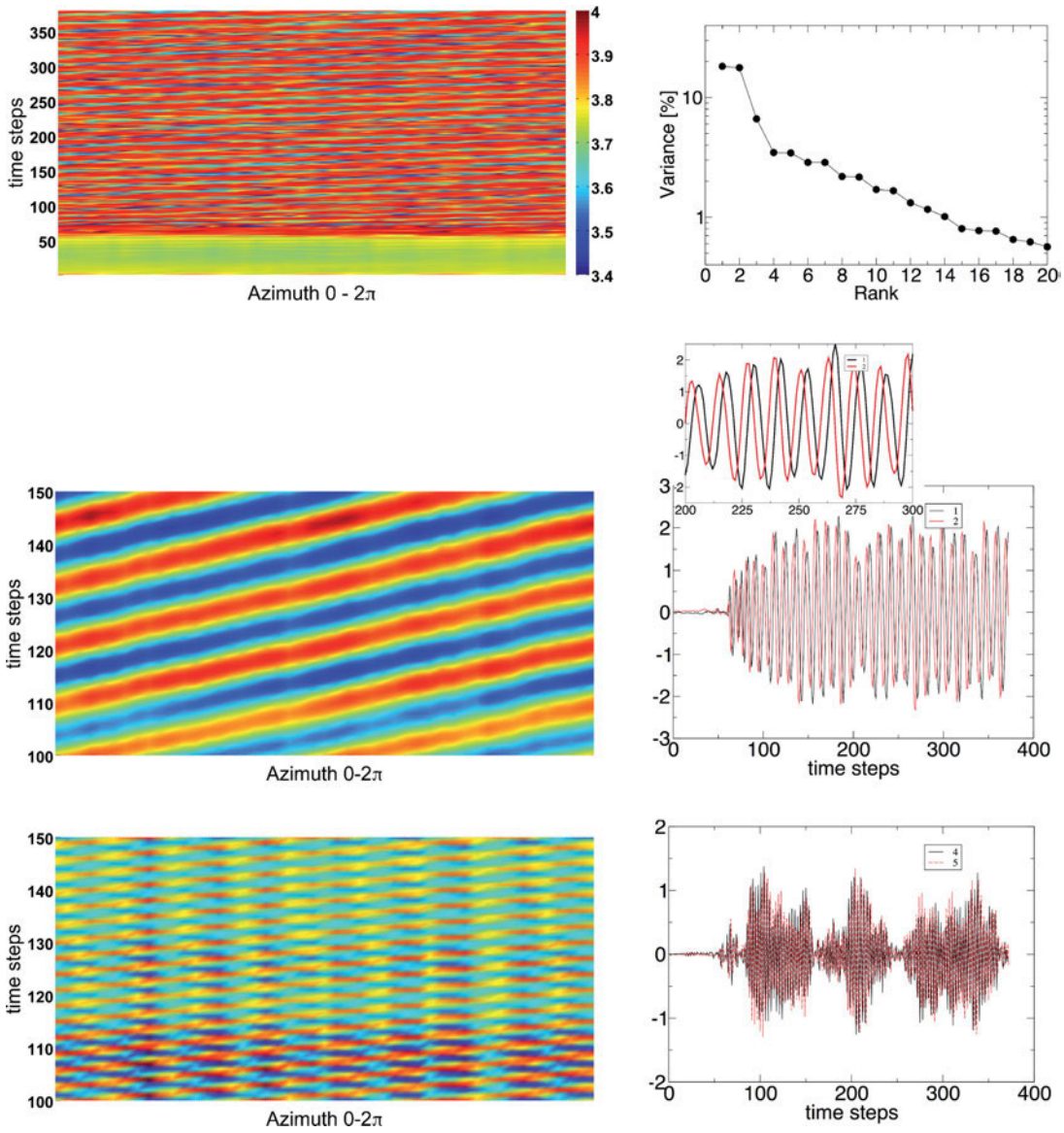

Figure 6: run *A*: Hovmoeller plot of the temperature data at mid radius at surface level (top left) and variance of the eigenvalue spectrum with the first 20 eigenvalues (top right). Single channel temporal PC 1 and 2 (center right) and temporal PC 4 and 5 (bottom right). The small panel shows an extract of the total time series of PC 1 and 2. Here, the phase shift between the two members of a PC pair is obvious. Reconstruction of the multichannel data time series using SSA components 1,2 (center left) and components 4,5 (bottom left). Note, that the multichannel reconstruction plots show extracts of the total time series, and that the single channel plots are normalized.

5 Discussion

The results found here at the four parameter points *A*–*D* reflect a typical sequence of wave number transitions usually found in measurement series in which the Taylor number is increased and the temperature difference is kept fix, i.e. where rotation rate is the variable parameter. Starting from a low rotation rate, one finds first the axisymmetric basic flow regime, followed by the wave flow regime and by the irregular flow regime at high rotation rates.

The flow phenomena under consideration in our numerical study are also observed in different experimental studies previously performed with the Cottbus laboratory model set-up. Specifically, VON LARCHER and EGBERS (2005a) presented series of experimental runs but for a slightly smaller temperature difference. In particular, complex mode interactions, as the $m = 2/3i$ pattern revealed at parameter point *B* in our numerical study, have been also presented in that paper at comparable parameter points, cf. Fig. 6 and 9 there. Furthermore, regarding our findings at parameter point *C*, HARLANDER et al. (2011) observed the coexistence of a weak wave mode and a dominating wave mode (at run *C* with $m = 3$ and $m = 4$ involved). Such a coexistence is often observed in regions close to a transition point within the baroclinic wave flow regime where the azimuthal wave number switches to the next higher one.

As already mentioned this numerical study is based on a reference experimental study from that parameter

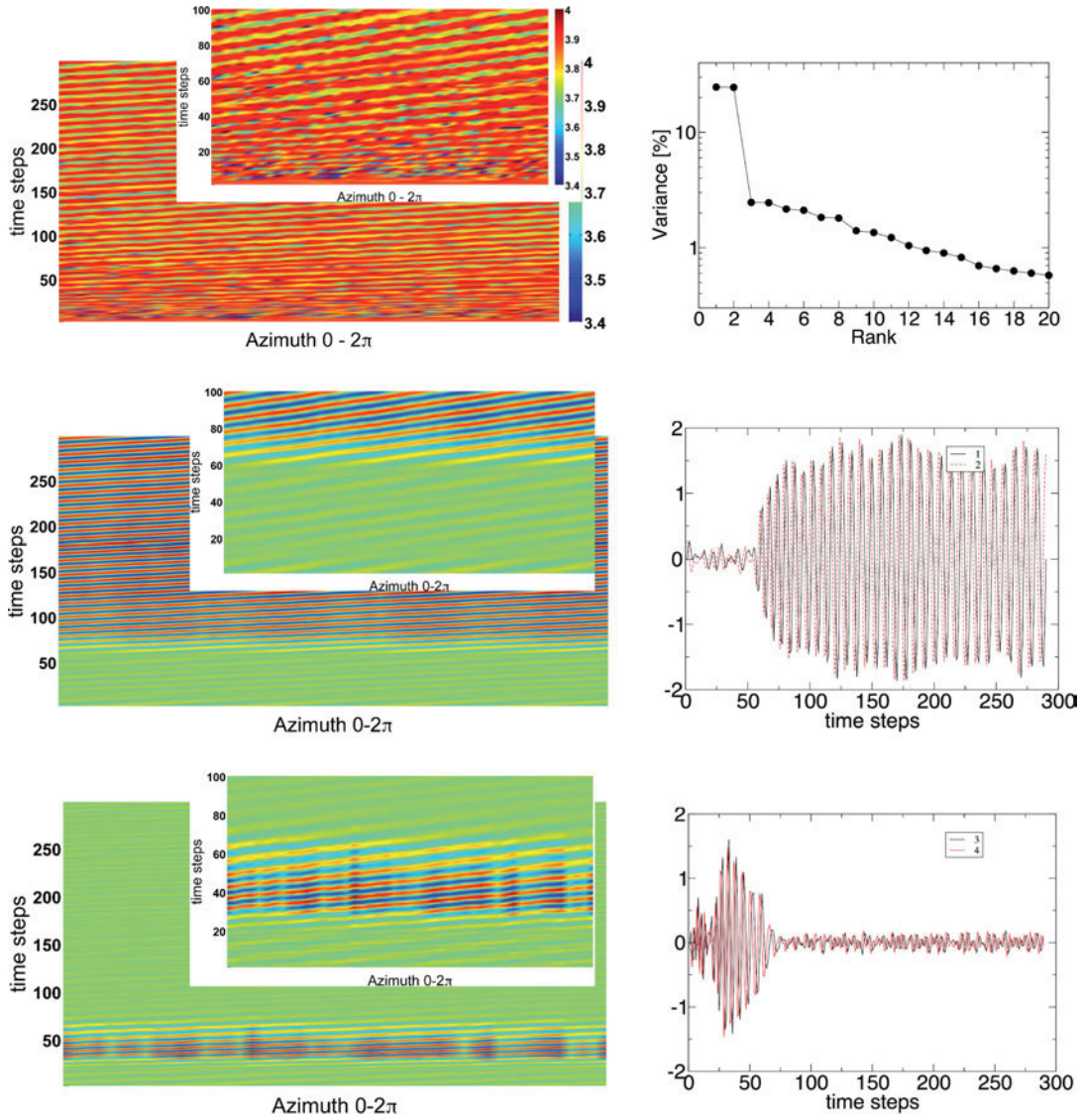

Figure 7: as in Fig. 6 but for run *C*. Here, SSA components 1,2 and 3,4 for the reconstruction of the data time series is used. Note also the extracts of the Hovmoeller plots in the smaller boxes.

points of interest were given for numerical research. It is interesting to note, that, apparently, a steady $m = 2$ wave mode but not a complex flow state was observed at parameter point *A* in the reference experiment run, cf. Table 1, the findings at the other parameter points are generally in good agreement.

The detected wave flow patterns are not only qualitatively in good agreement with the experiment results but also the drift rates fit generally well as documented in Table 1. In the model set-up of the thermally driven rotating annulus, drift velocities of flow patterns are determined by the thermal wind relation already mentioned at the end of Sec. 2.1. From this relation, it follows that the drift rate is inversely proportional to the rotation rate, $c \propto \frac{1}{\Omega}$, and, therefore, with (2.4) $c \propto \frac{1}{\sqrt{Ta}}$. Although the thermal wind relation is originally valid for the basic flow state found at low rotation rates only, the relation fits well also for a wide range of the baroclinic wave regime, as indicated in an experimental study by Sitte and Egbers (1999) (see also Hide (1958) and Fowlis and Hide (1965) for principal studies).

Our numerical experiments (Fig. 8, bottom panel) are in good agreement with the thermal wind relation except for run *D*. In the above mentioned experimental study performed by von Larcher in the 2000s, von Larcher (2007), using the reference model set-up as it is under consideration here, drift rates of wave patterns observed at a number of parameter points, covering a sequence from lower to higher rotations rates, were determined by visual inspection of the surface flow (Fig. 8, top panel). The experimental drift rates are partially in good agreement with the thermal wind relation (particularly between $2 \times 10^7 \leq Ta \leq 4 \times 10^7$) but at higher rotation rates ($Ta > 4 \times 10^7$), the trend fits better with exponent -0.4 rather than -0.5. The significant deviations for the $m = 2/3i$ flow state at smaller Taylor numbers are apparently dedicated to the complexity of the mode itself which makes it difficult to determine the drift rate from

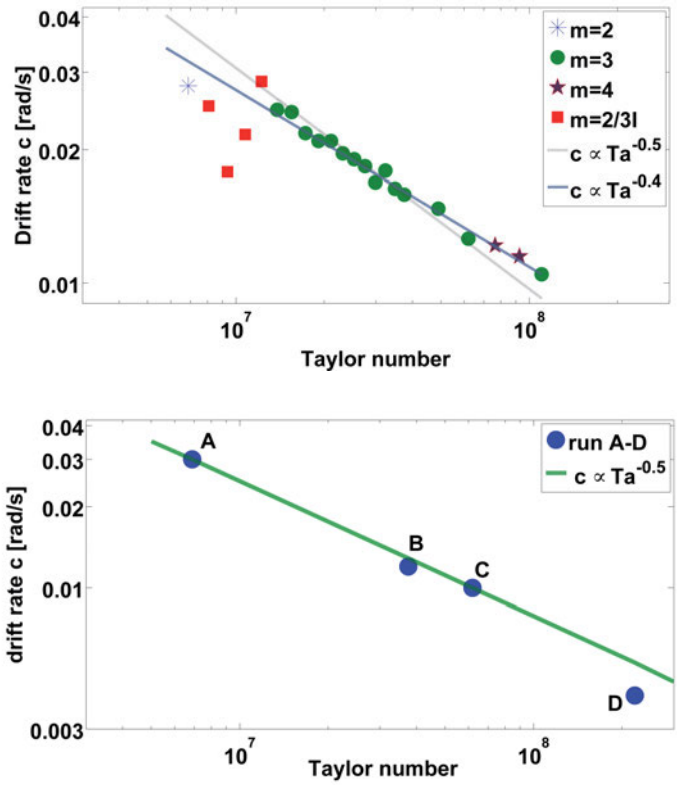

Figure 8: Top panel: drift rate of wave modes of different wave number m determined in an experimental study using the reference model set-up. Figure adapted from VON LARCHER (2007). Bottom panel: drift rates calculated from the numerical computations at run A–D and fit with $Ta^{-0.5}$.

visual inspection of the surface flow. Therefore, we conclude that the deviations from the thermal wind equation at smaller Taylor numbers are due to the complex flow state and the inspection technique. It is indeed interesting to note the deviations from the -0.5 exponent found at larger Taylor numbers. Those, apparently, systematic deviations might occur due to the growing influence of the centrifugal force. The thermal wind equation originally describes the vertical shear of the geostrophic wind which balances the Coriolis force and the pressure gradient force but which does not incorporate the centrifugal force. Thus, the onset of deviation from the -0.5 exponent might be interpreted as an indicator of the growing imbalance of the thermal wind due to growing centrifugal effects. However, this might be speculative at this point.

6 Concluding remarks

We have presented a numerical study of baroclinic flows in the classical thermally driven rotating annulus with a fixed temperature difference of $\Delta T = 8\,\mathrm{K}$ and rotation rate Ω as the variable parameter. We used the EULAG framework with immersed boundaries to solve the governing equations in the Boussinesq approximation. The approach was tested against results of an accompanying laboratory experiment. Advanced methods of data analysis, i.e. the multichannel singular systems analysis, were used to enable us detecting in particular complex flows where the established flow pattern is typically determined by a number of wave modes. In our study, we found steady wave patterns as well as mode interactions. The numerical results are in good agreement with the findings of the laboratory studies. As discussed here, this is in particular the case for the complex flows as well as for the drift rates of the dominant wave modes. The results presented here encourage us for the attempt to investigate chaotic flow patterns with the EULAG framework usually found at higher rotation rates where large-scale and small-scale flow features coexist. In that region, centrifugal effects become a dominating influence and turbulent features have to be taken into account. The EULAG framework appears well suited for that challenging task.

It is worth mentioning that the Cottbus laboratory experiment is used as reference experiment within the long-term priority programme *MetStroem*, and was therein used to support validation of model- as well as grid-adaptive numerical simulation concepts. Results of validation of particular numerical approaches developed within the framework of *MetStroem* against this reference experiment are shown in a forthcoming paper by VINCZE et al. which was recently submitted to *Meteorologische Zeitschrift*, cf. VINCZE et al. (2014a). Here, more results of our EULAG computations are discussed and compared with the outcome of other numerical flow solvers.

Acknowledgments

The work presented here has been conducted in an associated project within the priority programme 1276 MetStroem (*Multiple Scales in Fluid Mechanics and Meteorology*), http://metstroem.mi.fu-berlin.de, funded by the German Research Foundation (DFG). Andreas Dörnbrack gratefully acknowledges support by DFG (DO 1020/2). Thomas von Larcher further acknowledges funding via the DAAD-PROCOPE program 'baroclinic waves (ref. 55908227)'. The numerical data were generated using resources of the Department of Mathematics and Computer Science, Freie Universität Berlin, Germany.

References

Allen, M., L. Smith, 1996: Monte Carlo SSA: detecting oscillations in the presence of coloured noise. – J. Climate **9**, 3373–3404.

Broomhead, D., G. King, 1986a: Extracting qualitative dynamics from experimental data. – Physica D **20**, 217–236.

Broomhead, D., G. King, 1986b: On the qualitative analysis of experimental dynamical systems. – In: S. Sarkar (Ed.): Nonlinear Phenomena and Chaos. – Adam Hilger, Bristol, England, 113–144.

Cotter, C., P. Smolarkiewicz, I. Szczyrba, 2002: A viscoelastic fluid model for brain injuries. – Int. J. Numer. Meth. Fluids **40**, 303–311.

Dettinger, M., M. Ghil, C. Strong, W. Weibel, P. Yiou, 1995: Software expedites singular-spectrum analysis of noisy time series. – Eos, Trans. American Geophysical Union **76**, 12, 14, 21.

Elliott, J., P. Smolarkiewicz, 2002: Eddy resolving simulations of turbulent solar convection. – Int. J. Numer. Meth. Fluids **39**, 855–864.

Elsner, J., A. Tsonis, 1996: Singular spectrum analysis: a new tool in time series analysis – Springer, New York.

Fowlis, W.W., R. Hide, 1965: Thermal convection in a rotating annulus of liquid: effect of viscosity on the transition between axisymmetric and non-axisymmetric flow regimes. – J. Atmos. Sci. **22**, 541–558.

Früh, W.-G., P.L. Read, 1997: Wave interactions and the transition to chaos of baroclinic waves in a thermally driven rotating annulus. – Phil. Trans. R. Soc. A **355**, 101–153.

Fultz, D., 1951: Experimental analogies to atmospheric motions. – In: T. Malone (Ed.): Compendium of Meteorology. – Amer. Meteor. Soc.

Fultz, D., 1961: Development in controlled experiments on larger scale geophysical problems. – Advan. Geophys. **7**, 1–104.

Fultz, D., R.R. Long, G.V. Owens, W. Bohan, R. Kaylor, J. Weil, 1959: Studies of thermal convection in a rotating cylinder with some implications for large-scale atmospheric motions. – Amer. Meteor. Soc., Meteor. Monogr. **4**, 1–104.

Ghil, M., M.R. Allen, M.D. Dettinger, K. Ide, D. Kondrashov, M.E. Mann, A.W. Robertson, A. Saunders, Y. Tian, F. Varadi, P. Yiou, 2002: Advanced spectral methods for climatic time series. – Rev. Geophys. **40**, 3.1–3.41.

Goldstein, D., R. Handler, L. Sirovich, 1993: Modeling a no-slip flow boundary with an external force field. – J. Comput. Phys. **105**, 354–366.

Grabowski, W., P. Smolarkiewicz, 2002: A multiscale anelastic model for meteorological research. – Mon. Wea. Rev. **130**, 939–956.

Harlander, U., T. Larcher, Y. Wang, C. Egbers, 2011: PIV- and LDV-measurements of baroclinic wave interactions in a thermally driven rotating annulus. – Exp Fluids **51** (1), 37–49.

Harlander, U., J. Wenzel, Y. Wang, K. Alexandrov, C. Egbers, 2012: Simultaneous PIV- and thermography-measurements of partially blocked flow in a heated rotating annulus. – Exp Fluids **52**, 1077–1087.

Hide, R., 1958: An experimental study of thermal convection in a rotating fluid. – Phil. Trans. R. Soc. A **250**, 441–478.

Hide, R., 1969: Some laboratory experiments on free thermal convection in a rotating fluid subject to a horizontal temperature gradient and their relation to the theory of the global atmospheric circulation. – In: G. Corby (Ed.): The global circulation of the atmosphere. – Roy. Met. Office, London, 196–221.

Hide, R., P.J. Mason, 1975: Sloping convection in a rotating fluid. – Adv. in Phys. **24**, 47–99.

Hignett, P., 1985: Characteristics of amplitude vacillation in a differentially heated rotating fluid annulus. – Geophys. Astrophys. Fluid Dyn. **31**, 247–281.

Lu, H.-I., T.L. Miller, 1997: Characteristics of annulus baroclinic flow structure during amplitude vacillation. – Dyn. Atmos. Oceans **27**, 485–503.

Mann, M., J. Lees, 1996: Robust estimation of background noise and signal detection in climatic time series. – Climatic Change **33**, 409–445.

Mittal, R., G. Iaccarino, 2005: Immersed boundary methods. – Annu. Rev. Fluid Mech. **37**, 239–261.

Morita, O., M. Uryu, 1989: Geostrophic turbulence in a rotating annulus of fluid. – J. Atmos. Sci. **46**, 2349–2355.

Pedlosky, J., 1970: Finite-amplitude baroclinic waves. – J. Atmos. Sci. **27**, 15–30.

Pfeffer, R.L., S.R. Applequist, R. Kung, C. Long, G. Buzyna, 1997: Progress in characterizing the route to geostrophic turbulence and redesigning thermally driven rotating annulus. – Theor. Comput. Fluid Dyn. **9**, 253–267.

Prusa, J., P. Smolarkiewicz, A. Wyszogrodzki, 2008: Eulag, a computational model for multiscale flows. – Computers & Fluids **37**, 1193–1207.

Read, P., 1992: Rotating annulus flows and baroclinic waves. – In: E. Hopfinger (Ed.): Rotating Fluids in Geophysical and Industrial Applications. – Springer, Wien, New York, 185–214.

Read, P.L., 1993: Phase portrait reconstruction using multivariate singular systems analysis. – Physica D **69**, 353–365.

Read, P., M. Bell, D. Johnson, R. Small, 1992: Quasi-periodic and chaotic flow regimes in a thermally-driven, rotating fluid annulus. – J. Fluid Mech. **238**, 599–632.

Read, P.L., P. Maubert, A. Randriamampianina, W.-G. Früh, 2008: Direct numerical simulation of transitions towards structural vacillation in an air-filled, rotating, baroclinic annulus. – Phys. Fluids **20**, 044107.

Schröttle, J., A. Dörnbrack, 2013: Turbulence structure in a diabatically heated forest canopy composed of fractal pythagoras trees. – Theor. Comput. Fluid Dyn. **27**, 337–359.

Seelig, T., U. Harlander, R. Faulwetter, C. Egbers, 2013: Irregularity and singular vector growth in the differentially heated rotating annulus. – Theor. Comput. Fluid Dyn. **27**, 415–432.

Sitte, B., C. Egbers, 1999: LDV-measurements on baroclinic waves. – Phys. Chem. Earth (B) **24**, 437–476.

Smolarkiewicz, P., 1991: On forward-in-time differencing for fluids. – Mon. Wea. Rev. **119**, 2505–2510.

Smolarkiewicz, P., L. Margolin, 1997: On forward-in-time differencing for fluids: An eulerian/semi-lagrangian non-hydrostatic model for stratified flows. – Atmos-Ocean Special **35**, 127–157.

Smolarkiewicz, P., L. Margolin, 1998: MPDATA: A positive definite solver for geophysical flows. – J. Comput. Phys. **140**, 459–480.

Smolarkiewicz, P., R. Sharman, J. Weil, S. Perry, D. Heist, G. Bowker, 2007: Building resolving large-eddy simulations and comparison with wind tunnel experiments. – J. Comput. Phys. **227**, 633–653.

Vautard, R., M. Ghil, 1989: Singular-spectrum analysis in nonlinear dynamics with application to paleoclimatic time series. – Physica D **35**, 395–424.

Vautard, R., P. Yiou, M. Ghil, 1992: Singular-spectrum analysis: A toolkit for short, noisy chaotic signals. – Physica D **58**, 95–126.

Vettin, F., 1884: Experimentelle Darstellung von Luftbewegungen unter dem Einfluss von Temperatur-Unterschieden und Rotations-Impulsen. – Meteorol. Z. **1**, 227–230, 271–276.

Vincze, M., S. Borchert, U. Achatz, T. von Larcher, M. Baumann, C. Hertel, S. Remmler, K. Alexandrov, C. Egbers, J. Fröhlich, V. Heuveline, S. Hickel, U. Harlander, 2014a: Benchmarking in a rotating annulus: a comparative experimental and numerical study of baroclinic wave dynamics. – Meteorol. Z. **23**, xxxx–xxx, this issue

Vincze, M., U. Harlander, T. von Larcher, C. Egbers, 2014b: An experimental study of regime transitions in a differentially heated baroclinic annulus with flat and sloping bottom topographies. – Nonlin. Proc. Geophys **21**, 237–250.

von Larcher, T., 2007: Zur Stabilität barokliner Wellen im starr rotierenden Zylinderspalt. – VDI Verlag, Düsseldorf.

von Larcher, T., C. Egbers, 2005a: Dynamics of baroclinic instabilities using methods of nonlinear time series analysis. – In: J. Peinke, A. Kittel, S. Barth, M. Oberlack (Eds.): Progress in Turbulence II. – Proceedings of the iTi Conference in Turbulence. Springer, Berlin, Heidelberg, 304pp.

von Larcher, T., C. Egbers, 2005b: Experiments on transitions of baroclinic waves in a differentially heated rotating annulus. – Nonlin. Proc. Geophys. **12**, 1033–1041.

von Larcher, T., A. Fournier, R. Hollerbach, 2013: The influence of a sloping bottom endwall on the linear stability in the thermally driven rotating annulus with a free surface. – Theor. Comput. Fluid Dyn. **27**, 433–451.